Available online at www.sciencedirect.com
ScienceDirect
C. R. Physique 9 (2008) 303–322
COMPTES RENDUS PHYSIQUE
http://france.elsevier.com/direct/COMREN/

Materials subjected to fast neutron irradiation/Matériaux soumis à irradiation par neutrons rapides

Displacement damage and transmutations in metals under neutron and proton irradiation

Pavel Vladimirov [a,*], Serge Bouffard [b]

[a] *FZK, Institute of Materials Research I, P.O. Box 3640, 76021 Karlsruhe, Germany*
[b] *CEA/DRECAM, Centre interdisciplinaire de recherche ions lasers (CIRIL), BP 5133, 14070 Caen cedex 5, France*

Available online 18 April 2008

Abstract

The knowledge of the defect and impurity generation rates, as well as the defect spatial distribution, is the corner stone for the understanding of the evolution of material properties under irradiation. This knowledge is also an essential element for comprehensive experimental simulations of the behavior of irradiated materials.

In this article the interaction of neutron and proton irradiation with metals is discussed with respect to displacement damage production. Charged particle irradiation is also briefly illustrated. After discussion of the primary interaction of projectiles (neutrons, charged particles in general, and protons in particular) with target atoms/nuclei, we describe the interaction of a recoil atom with other target atoms resulting in the slowing down of the projectile, displacement damage, impurity atom production due to nuclear reactions, and the creation of atomic displacement cascades. Then the further evolution of defect structure is discussed. The next section, devoted to subcascade formation, is divided into two parts. The first experimental evidence of subcascade formation under neutron and charged particle irradiation is presented. Then the models of subcascade formation are described. Finally we review the models for the calculation of displacement damage and show how these models can be applied to displacement damage calculation under neutron irradiation with a demonstration of a real application of the methods discussed to several nuclear facilities. ***To cite this article: P. Vladimirov, S. Bouffard, C. R. Physique 9 (2008).***

Résumé

Dommage de déplacements et transmutations dans les métaux sous irradiation de neutrons et de protons. Connaître le taux de génération de défauts et d'impuretés ainsi que la distribution spatiale des défauts est la base de la compréhension de l'évolution des propriétés des matériaux sous irradiation. Cette compréhension est aussi essentielle à une définition exhaustive des simulations expérimentales du comportement des matériaux sous irradiation.

Dans ce papier on discute l'interaction des neutrons et des protons avec les métaux, et, la production de dommage de déplacements qui en résultent. On illustre aussi brièvement les irradiations par particules chargées. Après avoir discuté l'interaction initiale de la particule incidente (neutrons, particules chargées en général, et, plus particulièrement protons) avec les atomes et les noyaux cibles, nous décrivons l'interaction de l'atome de recul avec les autres atomes, qui a pour conséquence le ralentissement du projectile, la création de dommage par déplacements, la production d'impuretés par réactions nucléaires et la création de cascades de déplacements atomiques. On discute alors l'évolution ultérieure de la structure des défauts. La section suivante dévolue à la formation de cascades comprend deux parties. On présente d'abord les évidences expérimentales de formation de sous-cascades provoquées par l'irradiation de neutrons et de particules chargées, puis, les modèles de formation de sous-cascades. Finalement

* Corresponding author.
E-mail address: Pavel.Vladimirov@imf.fzk.de (P. Vladimirov).

1631-0705/$ – see front matter
doi:10.1016/j.crhy.2008.02.004

nous analysons les modèles de calculs de dommage de déplacements et nous montrons comment ces modèles peuvent être appliqués au calcul du dommage de déplacements sous irradiation de neutrons. L'application de ces méthodes au cas réel de plusieurs installations nucléaires est finalement présentée. ***Pour citer cet article : P. Vladimirov, S. Bouffard, C. R. Physique 9 (2008).***

Keywords: Neutron irradiation; Displacement damage; Atomic collision cascades

Mots-clés : Irradiation de neutrons ; Dommage de déplacements ; Cascades de collisions atomiques

1. Introduction

Fast neutron irradiation produces a modification of the lattice structure and generates gaseous transmutation products, both of which affect the mechanical, electrical and other physical properties of irradiated materials. It is well known that the effects of neutron irradiation cannot be fully simulated by ion irradiation. This difficulty results mainly from the differences in the distribution of energy transfer to the target atoms, as well as from the differences in the transmutation cross-sections. The defect spatial distribution and the relative concentration of impurities or gases produced by nuclear reactions depend on the projectile type and its energy, resulting in differences in defect clustering, bubble formation and segregation or dissolution rate. All these factors contribute directly to the microstructural evolution of materials. These effects have been extensively studied for fission neutron irradiation. Special efforts were undertaken to study experimentally the effects of fusion neutrons (see Section 5.1) although with a fluence much lower than that anticipated for the future fusion reactor. Presently, a dedicated intense neutron source with a fusion relevant neutron spectrum, displacement damage and gas production rates – the International Fusion Material Irradiation Facility (IFMIF) – is in the engineering validation and engineering design activities (EVEDA) phase [1]. However, before IFMIF will become available, fission test reactors and charged particle accelerators have to be used to simulate fusion neutron irradiation. With this in mind, damage calculations and modeling are indispensable tools required for the extrapolation of the results of fission and charged particle irradiations to the irradiation conditions of a fusion reactor. In this paper, we recall and discuss the process of displacement damage formation and further defect evolution, with a special emphasize on the specific features of fast-neutron and charged particle (mainly proton) irradiation.

2. Interaction of projectiles with target atoms

2.1. Interaction of neutrons with target nuclei

The displacement of atoms from their equilibrium lattice positions in a material irradiated with neutrons can occur by two different mechanisms. In the case of elastic (like billiard balls) or inelastic (where the target nucleus is left in an excited state) collisions, the target nucleus receives an impulse from the incident neutron and might be able to produce further displacements before being slowed down to rest in the lattice. The target nucleus in this process remains unchanged, although its de-excitation might occur either during slowing down or be delayed until it stops. Another mechanism of atomic displacement is due to neutron capture by the target nucleus and subsequent nuclear reactions. In this process, the target nucleus may undergo gamma emission, fission or produce a charged particle like hydrogen or helium. In this case, the reaction products may cause atomic displacements. If the reaction is exothermic and has a sufficiently high cross section for low energy neutrons, atomic displacements can be produced even by thermal neutrons, which do not have enough energy to generate defects in direct collisions. Typical examples of reactions in which this mechanism is operative are $B^{10}(n,\alpha)Li^7$, $Fe^{58}(n,\gamma)Fe^{59}$ and $U^{238}(n,f)$ [2–4]. An additional example of the exothermic reaction relevant for fusion blanket applications $Li^6(n,\alpha)H^3$, whose cross section is increasing as $1/\sqrt{E_n}$ with decreasing of neutron energy, was considered elsewhere (see e.g. [3]). The energy released in this reaction is divided between both reaction products (the tritium receives 2.6 MeV, and the alpha particle 2 MeV), which are producing small displacement cascades.

To have a deeper insight into this subject, the reader is referenced to the excellent review paper [4].

2.2. Interaction of heavy charged particles with target atoms

Ion irradiation is widely used for the surface modification of material properties and express simulation of the effects of neutron irradiation. Charged particles interact with target atoms by the long-range Coulomb forces, which are very effective in producing low-energy recoils in frequent distant collisions, while generating high-energy recoils in more infrequent close collisions. In this respect, Coulomb forces significantly diverge from the short-range nuclear forces acting between neutrons and target nuclei [5]. This fundamental difference in interaction results in: (i) a drastic decrease of the charged particle mean free path; (ii) a softer recoil spectrum; and (ii) an increase of the displacement damage rate. The last feature allows a fast accumulation of the required damage dose using charged particle accelerators. The ideal simulation of neutron irradiation with ions would require the same recoil spectra. However, this condition is never met and accurate recoil spectrum comparison is necessary to assess the significance of the difference. The process of charged particle slowing and defect creation is similar to that of recoil atoms, and is described in more details below (see Sections 3.1 and 3.2).

2.3. Interaction of high-energy protons with target nuclei

High-energy protons (typically several hundreds of MeV) impinging on the target material can be used to produce high energy neutrons for various applications. This principle is used in spallation neutron sources, where neutrons are produced by collisions of high-energy protons with a solid or liquid spallation target.

The reaction of high-energy protons with target nuclei can be considered as a two-step process [6,7]: a fast phase of nucleon–nucleon collisions, followed by a slow evaporation phase. A high-energy proton interacts directly with a single nucleon, since its wavelength is less than the distance between nucleons inside the target nucleus. While traveling through the nucleus, the proton can undergo several interactions. This phase, the so-called intra-nuclear cascade (INC), includes collisions of primary and secondary fast nucleons with other nuclei, as well as pion (π^+, π^-, π^0) production. During this phase, nucleons and their light clusters are emitted from the compound system. These particles have a high energy and are preferentially oriented in the direction of the primary proton beam. The emitted particles are able to react with other target nuclei in the same way as the incident proton. Therefore, a kind of nuclear cascade (analogous to the atomic displacement cascade described below) takes place. After this stage, the second slow evaporation phase begins, in which the highly excited pre-fragment releases its excess energy. De-excitation occurs either by evaporation of nucleons and nucleon clusters or by a fission-like breakup of the unstable pre-fragment into two or more fragments. During the evaporation phase, nucleons and light nuclei are emitted nearly isotropically.

The reaction path via the INC and evaporation is usually called spallation. High-energy neutrons produced via spallation are widely used for the investigation of the inner structure of solids or biological objects (spallation neutron sources, SNS) as well as being foreseen for burning long life radioactive isotopes from spent nuclear fuel (accelerator driven transmutations systems).

3. Interaction of recoil with target atoms

3.1. Nuclear and electronic energy losses

There are two major channels of energy loss by recoil moving in a solid target: (i) excitation and ionization of the target atom electrons; and (ii) kinetic energy transfer to the target nuclei (see e.g. [2,8]). In the second channel, the initial kinetic energy of the recoil is distributed among many target atoms. At high recoil energies, the electronic energy losses are much higher than those due to the nuclear collisions. So, in metals, if we neglect the effects observed at very high ion energies (about several MeV/amu), the moving ion is just dissipating its energy into the electronic subsystem until it slows down and the nuclear losses become important (see Fig. 1). With decreasing recoil energy the distance between nuclear collisions reduces until the recoil interacts with nearly every atom on its line of flight. At this point the collisions can no longer be considered as binary, as the energy is dissipated in a small volume, rather than transferred to some particular atom. The spatial region, where the most of the displacements are produced, is called a displacement spike.

This specific behavior of electronic and nuclear stopping powers gives rise to the splitting of high-energy cascades into smaller spatially localized subcascades, whose formation will be described later in more detail (see Section 5).

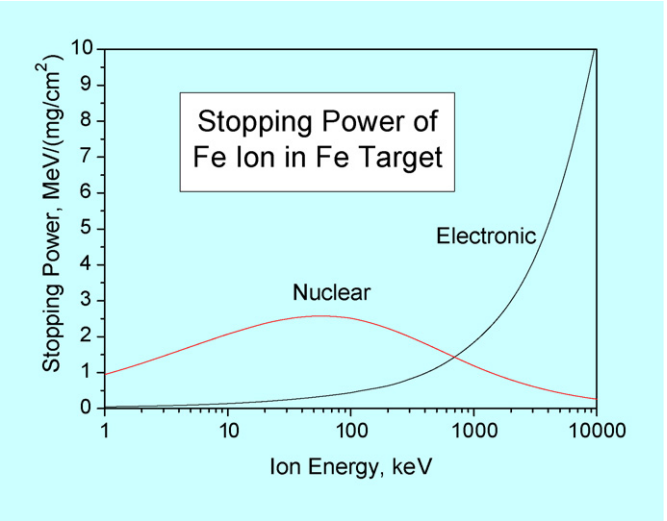

Fig. 1. Nuclear and electronic stopping power of an iron ion slowing down in an iron target calculated by SRIM [39].

Fig. 1. Pouvoirs d'arrêt nucléaire et électronique d'un ion incident Fe dans une cible de fer.

It should be mentioned that in metals the energy dissipated into the electronic subsystem is lost for the direct energy transfer to target atoms, resulting in the reduction in the number of displacements produced. However, this statement might be not true for the case of swift heavy ions (with energy of the order of MeV/amu), which are known to produce tracks even in metals [9,10].

3.2. Major defect formation mechanisms

Secondary displacements can be produced by direct collisions between recoils and target atoms. This defect production mechanism is always efficient, whatever the material nature. Another mechanism, which is important for dielectrics, is an energy transfer to electrons. This results in the ionization of the target atom and the formation of defects due to Coulomb repulsion. A detailed description of the mechanisms of the defect formation in insulators falls outside the scope of this paper.

The energy losses due to electron ionization and excitation also occur in metals, but usually they are lower than the energy transfer in atom–atom collisions, or of the same order. For example, at the maximum energy of recoil produced by 14 MeV neutrons in iron, the electronic and nuclear losses are comparable with each other (see Fig. 1). Only at very high energies of incident heavy ions (several Mev/amu) the excitation of the electronic subsystem becomes important. In this case, the material properties change significantly in the close vicinity of the heavy ion trajectory, resulting in formation of tracks [9,10].

Under neutron irradiation, the electronic excitations are significantly lower. A simple calculation performed with SRIM code shows that, for 14 MeV neutrons, only $\sim$30% of the recoil energy is released by electronic excitations. In this paper we will manly concentrate on metallic materials under fast neutron irradiation conditions where electron excitations do not produce displacement damage.

In some very peculiar cases, the radiation damage contribution from gamma rays in metals should be also considered [11], as it could be comparable with that from neutrons.

3.3. Atomic displacement cascades

By collisions with target atoms, fast neutrons create recoils – high-energy primary knocked-on atoms (PKA) – that initiate atomic displacement cascades. Therefore, many target atoms are knocked-on and displaced from their lattice positions, producing point defects: vacancies and interstitials (the so-called Frenkel pairs). A displacement cascade in solids develops as an avalanche involving an increasing number of displaced atoms. This picture is supported by numerous computer simulations using various approaches described below (see Section 6) as well as by experimental

Table 1
Time scales of the atomic displacement cascade development (see e.g. [12,13])

Tableau 1
Echelles de temps du développement de cascades de déplacements (voir par exemple [12,13])

Phase	Characteristic time
Collision stage	$\sim$0.1 ps
Relaxation stage	$< \sim$1 ps
Cooling/recombination stage	$< \sim$10 ps
Diffusion of freely migrating defects	$\sim 10^{-1}$–10^{6} s

observations (see Section 7). The moment when the maximum number of displaced atoms is reached is called the cascade peak time (or peak disorder time) and is typically between 0.2–0.5 ps (see Table 1), with up to several thousand atoms displaced for high-energy PKAs. During relaxation of this highly disordered state, a substantial recombination of vacancies and interstitials occurs in the cascade zone. Following in-cascade recombination and cooling down, the disorder is left in the form of isolated Frenkel pairs and small point defect clusters. Some of these clusters can already be observed at the end of the collision stage, while others are formed during the recombination stage. The recombination of the central region is generally completed after 1–2 ps. Further recombination and clustering takes up to about 3 ps for 5 keV cascade or longer for a higher PKA energy (see Table 1).

After the cooling stage, defect clusters take their equilibrium form and in up to 100 ps little or no change in the number and the size of defects, after the first 5 to 10 ps, occurs. The characteristic time of diffusion of freely migrating defects, which survived the in-cascade recombination, depends significantly on the material composition, irradiation temperature, microstructure (e.g., dislocation and irradiation induced loop density) and other factors, and varies, therefore, in a wide range, roughly indicated in Table 1.

4. Defect evolution

It should be emphasized that only a small fraction ($\sim$30% for the high-energy cascades [14]) of the point defects produced during the collision stage will survive after it. The central part of a cascade is very hot, with temperatures sometimes reaching the melting temperature of material. As a result, considerable point defect motion, recombination and clustering can occur inside cascade. The final configuration is generally a vacancy-rich core region surrounded by interstitial clusters.

For the development of the microstructure in irradiated materials not only production and survival of point defects are important, but also their in-cascade clustering. In fcc metals, vacancies tend to cluster in the form of a loop or a stacking fault tetrahedron, while in bcc metals they remain as single vacancies or small vacancy clusters [15]. Interstitial clustering was found to be also more pronounced in fcc than in bcc metals [15]; this was also confirmed by numerous computer experiments (see, e.g., [16,17]). It is believed that in-cascade vacancy and interstitial clustering can affect the kinetics of microstructure evolution [18,19]. For instance, the implications of one and two dimensional motion of a small interstitial for swelling or void lattice formation have been discussed already for decades (see, e.g., [16,20,21]).

One has to distinguish between: (i) the number of displacements in cascade, which corresponds to the peak disorder; (ii) the number of defects having survived after the recombination phase, being still localized in the cascade area; and (iii) freely migrating defects, which are available for diffusion in the bulk outside of the cascade. The last two values are different due to additional recombination, which occurs after cascade recombination. The number of freely migrating defects is important for further defect evolution.

In fact, both the number of defects escaping from the in-cascade recombination and the number of freely migrating defects are more or less fixed fractions of the total number of displacements. This justifies the fact that the physical property changes under irradiation correlate well with the displacement rate in terms of displacements per atom per second (see example in [4]).

5. Subcascade formation

5.1. Experimental data on subcascade formation under neutron irradiation

Extensive experimental studies using 14 MeV neutrons made in the 1980s and early 1990s in Japan, Europe and the USA offered deeper insight on displacement cascade development and provided experimental evidence for subcascade formation under high-energy neutron irradiation. Of particular importance was the Japan–USA Fusion Cooperation Program (1982–1986) which utilized a rotating target fusion neutron source, RTNS II, at the Lawrence Livermore National Laboratory (see e.g. [22]). The results obtained can be briefly summarized, as follows [23].

Neutron induced collision cascades produce a high concentration of vacancies localized near the core. These cascades are characterized by a high energy transfer from the incident neutron to the target atom. Large collision cascades are divided into small groups of dense collisions, called subcascades.

For fcc metals each vacancy cluster visible in TEM can be associated with one subcascade. In heavy fcc metals vacancy clusters are observed in the form of closely spaced groups, while in light-weight fcc metals, the clusters are widely separated from each other. Therefore it is difficult to identify to which subcascade they belong. In aluminium, vacancy clusters have been never observed to be formed by collision cascades. The reason is probably because of less dense collisions in cascades.

On the other hand, in bcc metals no vacancy clusters, which could be, with confidence, ascribed to collision cascades, were observed. As far as collisions are concerned, bcc and fcc metals should not differ substantially; one might assume that the difference is due to the point defect cluster formation as well as in their interaction with each other and/or with the microstructure existing before irradiation.

Interstitial clusters visible in the form of dislocation loops are commonly formed both in fcc and bcc metals under neutron irradiation. Most probably, they are formed by nucleation at small interstitial clusters formed in collision cascades and their subsequent growth is by absorption of freely migrating interstitials.

The effect of high-energy recoils on radiation damage is discussed elsewhere (see e.g. [24,25]).

The experimental evidence summarized above presents a solid background for the model of subcascade formation discussed in the following section.

5.2. Models of sub-cascade formation

Defect clusters formed in sub-cascades were observed using a transmission electron microscope (TEM) on neutron irradiated samples. If specimens are prepared with a considerable thickness gradient it is possible to detect more vacancy clusters near the thinner end of the specimen, while more interstitial clusters are observed near the thicker end. An explanation suggested is that in the thinner part of the sample, freely migrating interstitials rapidly escape to the free surface, while they stay available for interstitial cluster formation in the bulk [26]. It was assumed that defects produced at a small separation from each other belong to one cascade collision zone and are presumably produced by one neutron. It was found that the number of such zones is growing with the increase of PKA energy [26].

As can be seen in Fig. 1, an example of iron, the PKA with the energy greater than about 700 keV spends the most part of its energy on excitation and ionization of atomic electrons. Atom–atom collisions at such energies are very rare and subcascades generated by such collisions are well separated from each other (see upper part of the diagram shown in Fig. 2). After a considerable slowing down, the distance between atom–atom collisions become comparable with the size of the subcascade produced by secondary knocked-on atoms, and different subcascades begin to overlap [27] (see the lower part of Fig. 2). Roughly, one can assume that for the energies below some threshold value only one cascade zone, consisting of several overlapped subcascades, is formed. Using this threshold energy, the number of separated cascade zones can be estimated. Several approaches were developed for assessment of the number of subcascades. Their detailed discussion is outside of the scope of the present paper and can be found elsewhere [27–30].

6. Models for calculation of displacement damage

The problem of radiation damage simulation and evaluation of irradiation exposure parameters was studied extensively. At least five major approaches to the problem can be mentioned here.

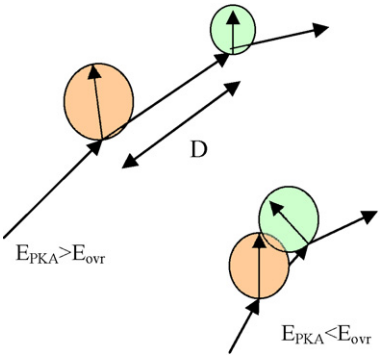

Fig. 2. Schematic representation of subcascade formation: at high PKA energy (the upper left part of the diagram) subcascades are separated, while after slowing down (the lower right part) they overlap.

Fig. 2. Représentation schématique de la formation de sous-cascades : si l'énergie du Premier Atome Frappé (PAF) est élevée (en haut et à gauche du diagramme), les sous-cascades sont séparées, par contre après ralentissement (en bas à droite du diagramme) il y a recouvrement des sous-cascades.

All the calculation methods described below assume a threshold energy atom displacement model. The kinetic energy of incident particle can be transmitted to the target atom in collision and if the transferred energy exceeds a certain threshold, the target atom is displaced and a stable pair of vacancy and interstitial sites (usually called Frankel pair) is created.

The most simple analytical approach to radiation damage calculations for monatomic materials was initially proposed by Kinchin and Pease [31] and further developed by Torrens, Robinson and Norget. The latter is now commonly referred as the NRT standard [32,33]. This standard is widely used as an internationally agreed irradiation exposure parameter – displacements per atom (dpa). It describes the formation of displacement damage without considering any type of defect recombination and the secret behind its success in describing correlations between material property changes and the irradiation dose expressed in dpa was discussed in Section 4.

In this approach, the radiation damage from a PKA of energy T is determined by the part of its energy E^*, spent in the displacement damage and is defined as the initial recoil energy minus the energy spent for electron excitation and ionization by the initial and all the secondary recoils produced in the atomic collision cascade. As soon as E^* is estimated, one can calculate the total number of defect pairs produced by PKA in accordance with the following simple relation:

$$\nu(T) = \begin{cases} 0, & T < E_d \\ 0.8E^*(T)/(2E_d), & T > E_d \end{cases} \tag{1}$$

Here E_d stands for the threshold displacement energy of the target atom from its lattice site.

It was recognized from fundamental experimental studies and computer simulations that the dpa value should be corrected to account for in-cascade recombination. However, this correction has not yet been incorporated in the dpa standard. Indeed, evidence from various experiments suggests that in spite of its limitations, the dpa parameter provides an adequate exposure parameter, correlating with changes in material properties.

The integral equation formalism was proposed first by J. Lindhard [34–36], which allows inclusion of the electronic stopping power effect on cascade development in monatomic solids. Later, this approach was extended by D. Parkin and C. Coulter [37] who proposed the way to numerically solve this problem for multi-component materials. A computer code realizing this approach was developed by L. Greenwood [38].

Another approach consists in the Monte Carlo simulation of each slowing primary recoil. It is based on the binary collision approximation, where collision events are considered to be independent from each other and no collisions between moving species are allowed. All Frenkel pairs generated are considered as stable, although a particular pair could be removed later if the distance between vacancy and interstitial sites is less than given recombination radius. The recombination radius is considered as a free parameter of the model. Such an approach provides detailed information on the resulting spatial damage distribution. The most well known realizations of the approach is the TRIM[1] [39] and MARLOWE [40] codes.

[1] The latest version (SRIM-2008) is available at http://www.srim.org/.

The molecular dynamics (MD) method is the only one which is able to include dynamical effects like collisions between moving atoms as well as non-binary collisions, which are important near the end of the recoil range. Defect recombination is also naturally included. Yet good interatomic potentials are necessary to obtain meaningful results. However, high-energy cascades cannot be calculated by MD methods due to the limitations in computer time and available memory. Up to now the state of the art MD calculations are still limited to ∼100 keV recoil energy.

In addition, there exists the fifth approach based on the solution of the Boltzmann transport equation for moving particles. It takes the middle ground between analytical and MC approaches mentioned above both for the amount of the available information and for computing power demands.

The approach based on the direct solution of Boltzmann transport equation is suitable for the most cases of stopping and damage calculations in compound targets (see e.g. [41]). Besides the total number of displaced atoms, the number of displaced atoms of each species is available, which makes this approach attractive for multi-component targets, where an analytical method is inapplicable.

7. How to calculate damage in neutron irradiated materials (theory)

Calculation of displacement damage produced by neutron irradiation is usually performed in two steps (see e.g. [42] for more details). First, the primary knock-on atom (PKA) spectrum for a specific neutron environment is calculated using neutron-target interaction cross sections. The NJOY code [43] is, in particular, very useful for getting access to the evaluated nuclear data libraries written in ENDF/B format. The second step consists in the calculation of PKA transport and of the associated radiation damage using the methods discussed above.

For the defect production by atom–atom collisions, the main input data are the primary-recoil energy spectra or, in other words, the energy-transfer cross-section and, of course, the displacement threshold energy. The displacement threshold energy depends on the material and on the direction of the atom ejection [44]. However, for the calculation of the number of displacements, one considers only the direction averaged threshold energy value. For most important elements the threshold values are specified by the standard as, for example, $E_d = 40$ eV for iron [45]. At the first glance, this value differs significantly from the minimum threshold displacement energy, in iron reported to be about 17 eV [46]. However, after averaging the threshold energy over the directions of incident atom it appears to be rather close to the value specified by the standard (see e.g. [47]).

There are several codes useful for practical applications (e.g., NJOY [43], SPECTER [38] or NPRIM [48]) that convolute the neutron spectrum with neutron cross sections to obtain the primary knock-on atom spectrum and calculate the displacement damage rate. These codes are able to process elastic and discrete inelastic collisions (where nucleus excitation level is known and the energy and momentum conservation lows can be applied) as well as some charged particle production reactions. The results presented in Section 8 were obtained using NJOY code for the PKA spectra calculation and Boltzmann transport equation solver BOLT [49] for the displacement damage calculations.

7.1. Damage cross sections

For monatomic targets a notion of damage cross section based on the simple analytic approach (see Eq. (5)) is very useful.

$$\sigma_d(E) = \int \nu(T) \frac{\mathrm{d}\sigma(E,T)}{\mathrm{d}T}\,\mathrm{d}T \tag{2}$$

Here $\frac{\mathrm{d}\sigma(E,T)}{\mathrm{d}T}$ is a differential cross-section of the energy transfer T to target recoil from incident particle with energy E.

It should be noted that this approach is often used also for the multi-component targets. However, it will give a reasonable approximation for compound material only if the masses and displacement thresholds of the various elements in the target are similar. Otherwise, more complicated approaches developed for multi-component materials should be used.

7.1.1. Neutron damage cross sections

A typical damage energy cross section calculated by NJOY code, using NRT approach described above, is shown in Fig. 3. This entity is in fact the damage cross section defined by Eq. (2) multiplied by a factor $2E_d/0.8$ (cf. Eq. (1)).

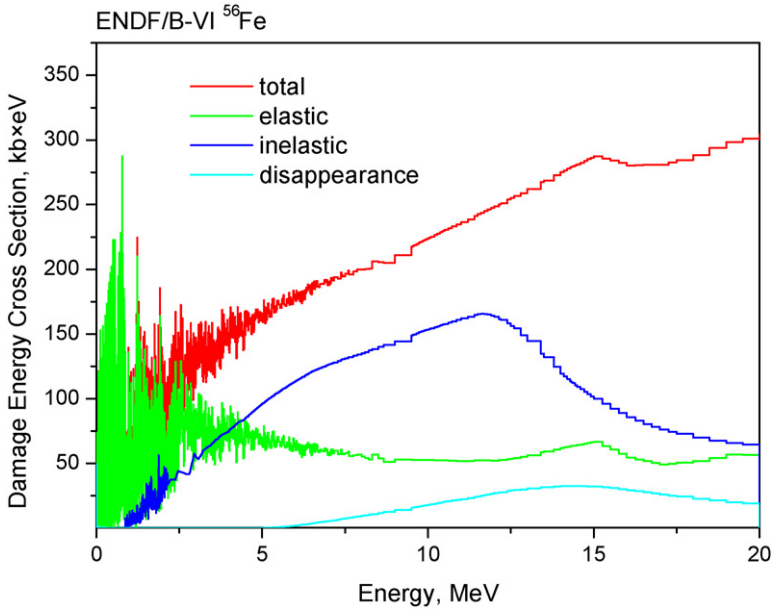

Fig. 3. Damage energy production cross section (kbarn eV) for ^{56}Fe calculated by module HEATR from NJOY code.

Fig. 3. Section efficace de production du dommage (kbarn eV) en fonction de l'énergie d'un ion incident ^{56}Fe. Le calcul est fait en utilisant le module HEATR du code NJOY.

For monatomic materials, this value is more convenient as it does not depend on the threshold displacement energy. Elastic, non-elastic and neutron disappearance channels of damage production are shown separately. Above 4 MeV non-elastic damage provides major contribution to damage production.

7.1.2. Neutron and proton damage cross section at high energies

Damage produced by neutrons and by charged particles is usually calculated by folding the incident particle energy spectra with respective damage production cross sections. Several proton and neutron damage production cross sections for the energy range up to 25 GeV in iron are shown in Fig. 4.

As can be seen from Fig. 4, the neutron damage cross sections from various sources differ from each other by the degree of detail with which numerous nuclear resonances are given. However, all of them produce very similar net damage rates as far as peaks and drops balance each other.

It is well known that under accelerator irradiation, charged particles produce significant damage near the end of their range. This can be explained by the fact that at high energies the electronic stopping power is dominating the nuclear one, which becomes significant only near the end of the recoil range (see discussion in Section 3.1). It should be noted that nuclear stopping is due to substantial energy transfer in atom–atom collisions, i.e. due to Coulomb scattering. Therefore charged particle damage is produced very inhomogeneously and its maximum is situated at a certain depth in the irradiated sample.

As can be seen from Fig. 4 the proton damage cross section taken from the BISERM2 [50] library has a pronounced maximum at 4 keV, where it is more than two orders of magnitude higher than the damage cross section in the spallation region (>100 MeV). On the other hand, this effect caused by Coulomb scattering, is not properly taken into account in LAHET [53] (a Monte Carlo code for the transport of high-energy nucleons, mesons and pions), where the proton damage cross section vanishes for energies less than 100 MeV. Fortunately, this fact did not affect the calculations presented in Section 8 due to the rapid drop of the proton spectra in the relevant energy range.

7.2. PKA spectra

For a simple estimation of the damage induced by neutron irradiation, in the first approximation the cross-section of atom–atom collisions can be considered to be of a hard-sphere type $\frac{\mathrm{d}}{\mathrm{d}T}\sigma(E_n, T) = \frac{\pi(r_n+r_t)^2}{T_{\max}}$, where r_n and r_t are,

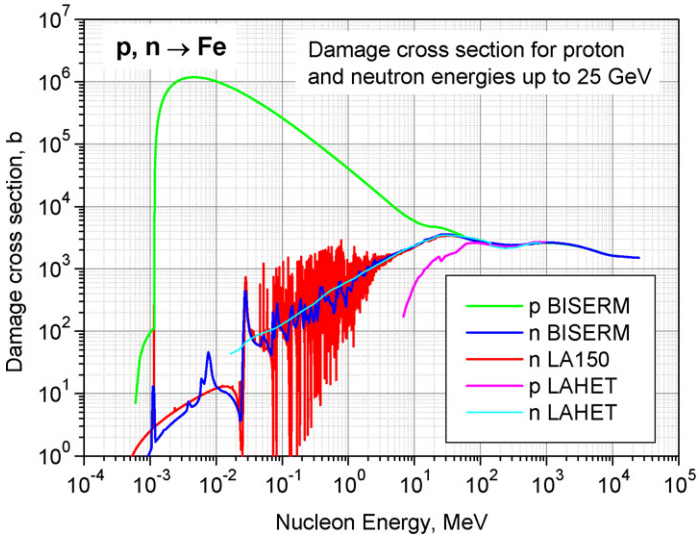

Fig. 4. Damage production cross sections for protons and neutrons taken from BISERM2 [50] and LA150 [51] nuclear data libraries and as provided by LAHET code [52].

Fig. 4. Section efficace de production de dommage par protons et neutrons obtenue à partir des bibliothèques de données nucléaires BISERM2 [50] et LA150 fournies par le code LAHET [52].

respectively, the radius of the neutron and of the target nucleus, and $T_{\max}$ the maximum energy transferred during a collision, $T_{\max} = \frac{4M}{(M+1)^2} E_n$ for a neutron of energy E_n and an ion of mass M (expressed here in the units of the neutron mass). This cross-section favours the large energy transfer to the target atom. It is particularly visible if we compare different ion cross-sections (Fig. 5). The total cross-section is smaller for neutron (typically 1.4 barn for neutron on iron) than for an ion which interacts through a screened Coulomb potential (∼2230 barns for a 14 MeV proton or ∼95 Mbarns for a 1 MeV Fe). For the three preceding examples, which have been chosen because they give the same $T_{\max}$, the mean number of displacement per PKA are 5800, 15 and 3.2 for a 14 MeV neutron, 1 MeV Fe ion and 14 MeV proton respectively.

For neutron irradiation, we have also to take into account the neutron energy spectra. For example, in the blanket structure of DEMO, the neutron spectra could be assumed to be constituted by a wide-energy distribution which decreases as $\sim 1/E$ [54,55]. The contribution to the damage of the peak around 14 MeV is small; however, the high-energy neutrons are responsible for the increased transmutation and gas production rates. Assuming this energy distribution, the cross-section for PKA creation looks like more that of the ions. The mean number of displacement per PKA decreases from 5800 to 390.

In practice it is important to use more complicated neutron cross sections (as was discussed previously in Section 7.1.1) and neutron energy spectra to assess the displacement damage more carefully.

Neutron interaction cross section should be convoluted with neutron spectrum to provide the number of i-type PKA per unit energy:

$$q_i(T) = \int_0^{T_m} \mathrm{d}E_n \, \Phi(E_n) N_i \sum_r \frac{\mathrm{d}\sigma_i^r(E_n, T)}{\mathrm{d}T} \tag{3}$$

where $\Phi(E_n)$ is a differential energy spectrum of neutrons, $\frac{\mathrm{d}\sigma_i^r(E_n,T)}{\mathrm{d}T}$ is a differential cross-section of the energy transfer T to the i-type recoil from neutron with energy E_n in nuclear channel r.

Typical PKA spectra calculated for various nuclear facilities discussed in detail later in Section 8 are presented in Fig. 6. Being normalized, these PKA spectra give a probability to observe a given energy transfer to a target atom.

Hard (fast neutron induced) and soft (e.g. electron irradiation induced) primary knock-on atom (PKA) spectra can produce very different damage morphologies. Low-energy recoils produce mainly Frenkel defects, that is, isolated pairs of vacancies and interstitials. A significant fraction of these defects survives recombination and can be involved

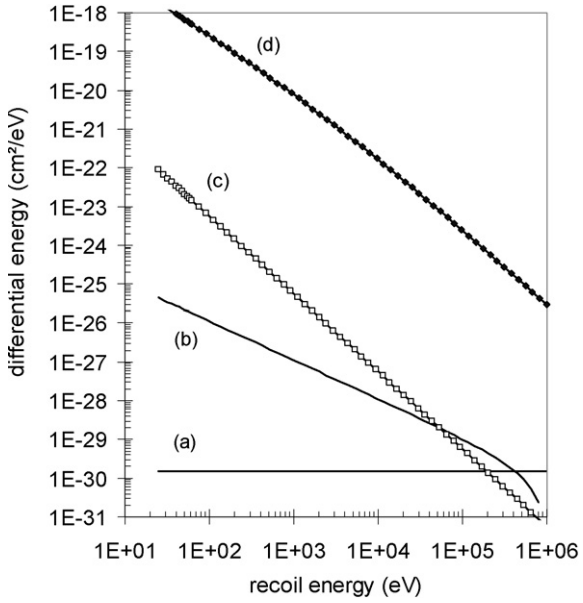

Fig. 5. Differential cross-section of PKA production in iron target (a) for 14 MeV neutron, (b) for a typical $1/E$ neutron spectra, (c) for 14 MeV proton, (d) for 1 MeV Fe ion.

Fig. 5. Section efficace différentielle de production de PAF dans une cible de fer irradiée par (a) des neutrons de 14 MeV, (b) des neutrons d'un spectre typique variant en $1/E$, (c) des protons de 14 MeV, (d) des ion de fer de 1 MeV.

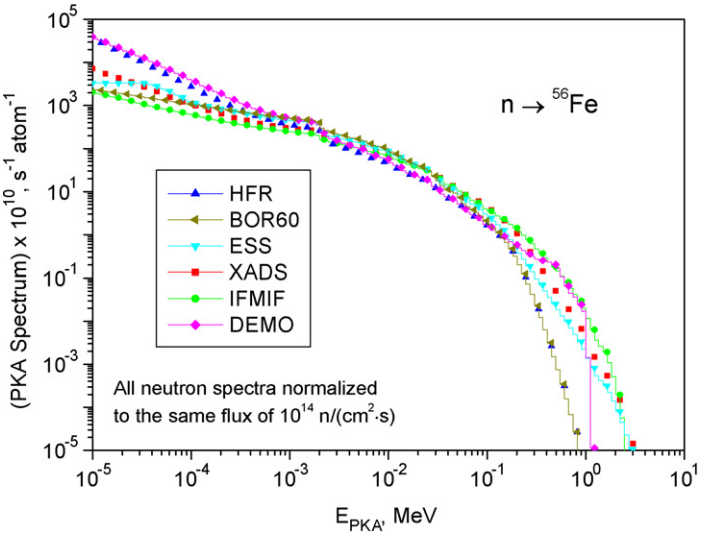

Fig. 6. Neutron induced PKA spectra of ^{56}Fe for several nuclear facilities discussed in Section 8.

Fig. 6. Spectres de PAF induits dans du ^{56}Fe par plusieurs installations nucléaires discutées en Section 8.

in the further defect kinetics. On the other hand, high-energy recoils generate atomic collision cascades in which a high fraction of the defects recombine during collision and cooling phases. For a PKA with the energy higher than some critical value (according to different authors it is in the range of 10–20 keV for Fe, see e.g. [56]), the formation of several sub-cascades is more probable.

To characterize the entire PKA spectrum, a cumulative damage production function $W(T)$, which represents the fraction of damage energy released by all PKA recoils with recoil energies less than given recoil energy T, is often

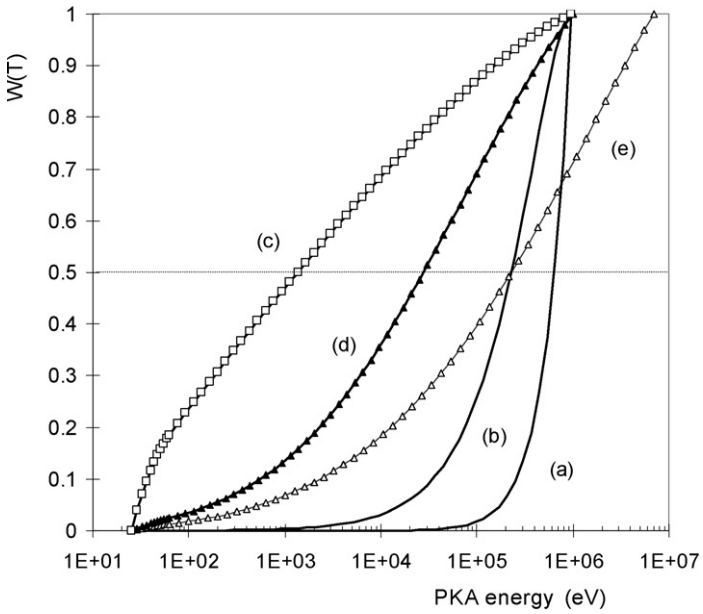

Fig. 7. $W(T)$ function for iron target irradiated by (a) for 14 MeV neutron, (b) for a typical fission neutron spectra, (c) for 14 MeV proton, (d) for 1 MeV Fe ion, (e) 20 MeV Fe ion.

Fig. 7. Fonction $W(T)$ pour une cible de fer irradiée par (a) des neutrons de 14 MeV, (b) des neutrons de fission de spectres typiques, (c) des protons de 14 MeV, (d) des ions Fe de 1 MeV, (e) des ions Fe de 20 MeV.

used. The cumulative damage production function thus depends on neutron spectrum and can show a difference in damage morphology for different irradiation sources.

$$W(T) = \frac{1}{G} \int \Phi(E) \int_{E_d}^{T} \frac{\mathrm{d}\sigma_{\mathrm{PKA}}(E, T')}{\mathrm{d}T} \nu(T') \,\mathrm{d}T' \,\mathrm{d}E \tag{4}$$

Here G is total displacement damage rate as defined by Eq. (5).

In Fig. 7, the function $W(T)$ is plotted for the three particles mentioned above with the same $T_{\max}$ ((a), (c), (d) curves), for a $1/E$ neutron distribution ((b)) and a high-energy ion which has the same $T_{1/2}$ value ((e)) ($T_{1/2}$ is the recoil energy for which a half of the total number of displacements is produced by the PKA with energies lower than $T_{1/2}$: $W(T_{1/2}) = 0.5$). The lower $T_{1/2}$ is, the harder the recoil spectrum.

These curves indicate that under neutron irradiation, defects are mainly produced in large cascades: half of the displacements are produced by PKA which have energies greater than 100 keV. Using ion irradiation, it is thus possible to produce the same number of displacements, but not the same spatial defect distribution as by neutrons. Under ion irradiation, weak energy transfers are more preferred, with two consequences: more isolated defects avoid recombination before the end of displacement cascade and fewer defects are clustered. The experimental results as well as molecular dynamic simulations confirm this increasing fraction of defects in clusters when the mean transferred energy increases (see for example [57–59]). The mean size of the clusters increases at the same time. These differences can affect kinetics of material behavior under irradiation: atom diffusion is facilitated by the presence of freely migrating defects (so called irradiation enhanced diffusion), on the other hand the increase of the number and of the size of the cascades could modify the formation and the stability of the clusters of defects and impurities or of the gas filled bubbles.

However, the difference can be tolerated for the experimental simulation by ion irradiation of the effects of neutron irradiation. Indeed, the fragmentation of large cascade in sub-cascade has been demonstrated above (see Section 5). The typical energy of the sub-cascade formation is about 10–20 keV [56]. It was confirmed by both molecular dynamic simulations [56,59] and experiments [60] that the efficiency of defect formation (the number of free defects normalized by the number of displacements) decreases down to 0.3 at 10 keV with increasing the mean PKA energy. For higher

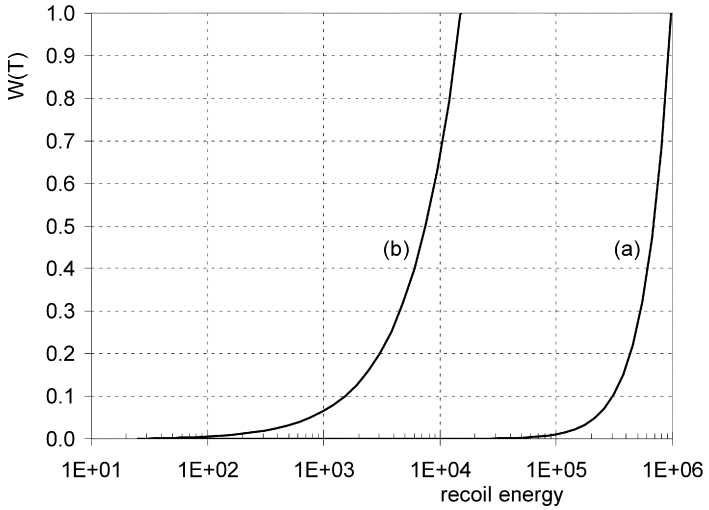

Fig. 8. $W(T)$ function for iron target irradiated by 14 MeV neutron, (a) classical calculation (b) in considering the PKA of energy greater than 15 keV as independent projectiles.

Fig. 8. Fonction $W(T)$ dans le cas d'une cible de fer irradiée par des neutrons de 14 MeV, (a) calcul classique, (b) en considérant les PAF d'énergie supérieure à 15 keV comme indépendants du projectile incident.

energies this value remains constant. Thus, the high-energy PKA can be considered as a new projectile: the material suffers a complex irradiation with neutrons and ions which have the same mass as target atoms and an energy spectrum varying between a critical energy E_c and $T_{\max}$.

If the PKA above E_c are considered as projectiles, the $W(T)$ function can be written as follows:

$$W(T) = \frac{1}{\sigma_d} \int_{E_d}^{T} \nu(T) \left[\sigma(E_p, T) + \frac{1}{\int_{E_d}^{T_{\max}} \sigma(E_p, T)\,\mathrm{d}T} \int_{T_c}^{T_{\max}} \chi(U, T)\sigma(E_p, U)\,\mathrm{d}U \right] \mathrm{d}T$$

where $\chi_{(U,T)}$ is the energy cross-section for production of secondary knock-on atoms of energy T by a PKA with energy U. The result of such integration is represented in Fig. 8 for the case of 14 MeV neutron irradiation. Fig. 8 shows that in the case where the high-energy PKA are considered as new ion projectiles, the PKA spectrum hardens significantly: $T_{1/2}$ is two orders of magnitude lower than in the case when all PKA are treated together (see Eq. (4)).

It is clear that computer simulation techniques need to be further developed to relate more precisely the relationship between the neutron spectrum, damage morphology and mechanical properties of irradiated materials.

7.3. Displacement damage and gas production

Total displacement damage rate can be calculated using the simple analytical cascade model (see Eq. (5)) as follows:

$$G = \int \Phi(E) \int_{E_d}^{T_m} \frac{\mathrm{d}\sigma_{\mathrm{PKA}}(E, T')}{\mathrm{d}T} \nu(T')\,\mathrm{d}T'\,\mathrm{d}E \tag{5}$$

Using Eq. (2) for the damage cross section, this equation can be rewritten as

$$G = \int \Phi(E)\sigma_d(E)\,\mathrm{d}E \tag{6}$$

In these equations damage rate is expressed in displacements per target atom per unit time (dpa/s). Therefore this value is independent of the target density.

The gas production rate can be calculated using similar convolution formula, where the damage production cross section is substituted by that for the gas production.

8. Damage calculation in neutron irradiated materials (real life example)

As an example of damage calculations a comparison of structural material irradiation conditions for several neutron environments will be presented in this section, which extends the analysis performed in Ref. [55].[2]

8.1. Nuclear facilities considered

In the last decades, significant efforts have been spent for the design of a number of novel nuclear facilities. The major role among them belongs to the fusion prototype reactors ITER and DEMO aimed at demonstrating the technical feasibility of electrical power production by means of the (d, t) fusion reaction. On the other hand, several accelerator-based facilities have been designed either in support of the fusion material development program (IFMIF), for the incineration of nuclear wastes (XADS) or for other scientific purposes (SNS, ESS).

In the present section, several nuclear facilities are compared with respect to material irradiation conditions. Different types of facilities have been considered: the intense stripping neutron source IFMIF, spallation sources ESS, fusion prototype reactor DEMO and fission material testing research reactors HFR and BOR-60.

While the purposes of the facilities considered in this work are quite different, there is a common problem of development and testing of the structural materials capable of sustaining hard operating conditions. Assessment of the irradiation conditions for nuclear facilities is required by designers and material scientists to make an optimum and safe choice of the structural materials for each facility.

The *Future Demonstration Power Reactor – DEMO* is a magnetically confined fusion prototype reactor with a power of 2–4 GW and an expected wall loading of the order of 2–3 $\mathrm{MW/m^2}$. The first inner wall of the facility is exposed to a high neutron flux, resulting in about 30 dpa per full-power year of operation. In this work, material responses were calculated at the position of the maximum neutron irradiation load on the central outward segment of the DEMO Helium-Cooled Pebble Bed Blanket [61].

The *International Fusion Materials Irradiation Facility* – IFMIF is the accelerator based deuterium-lithium (d-Li) stripping neutron source for the production of high-energy neutrons at sufficient intensity to test samples of fusion candidate materials up to about the full lifetime of their anticipated use in fusion energy reactors. Two deuteron beams (40 MeV, 2×125 mA) are striking a common liquid lithium target and produce high-energy neutrons with a peak energy around 14–16 MeV permitting irradiation of material samples with a damage rate higher than 20 dpa/fpy in 0.5 l volume.

The description of the geometry model and the details of neutronics analysis for IFMIF High and Medium Flux Test Modules (HF & MFTM) can be found elsewhere [62–64].

The *European Spallation Source* – ESS is a spallation neutron source driven by a proton linear accelerator (LINAC) with a beam energy of 1.33 GeV and a beam power of 10 MW [65]. It features two target stations, both equipped with a liquid mercury target and operating with 5 MW beam power.

Since it was suggested to use spallation sources for fusion materials testing to bridge the time until the IFMIF source is available [66], a related feasibility study has been performed [67]. As a result, for material irradiation in the ESS a useful "high-flux" volume of about 0.83 l at the out-of-target reflector position of the short pulse target station has been identified [68]. The geometry model description and neutronics analysis of the ESS can be found elsewhere [68].

Fission reactors: The High Flux Reactor (HFR) at Petten, the Netherlands, is a light water moderated and cooled multipurpose materials testing reactor with a thermal power of 45 MW. The BOR-60 facility at Dimitrovgrad, Russia, is a fast, sodium-cooled reactor designed to test fuel elements and structural materials. At present, both reactors are extensively used for the irradiation testing in the fusion material program.

The *Experimental Accelerator Driven System* – XADS, aimed at the reduction of radiotoxicity of spent nuclear fuel by means of their incineration, is considered in this paper for comparison only, as the irradiation conditions of the hot window material [69,55] are mainly determined by the proton beam rather than by spallation neutrons.

[2] This section includes some text extracts reproduced from [55] with permission from Elsevier.

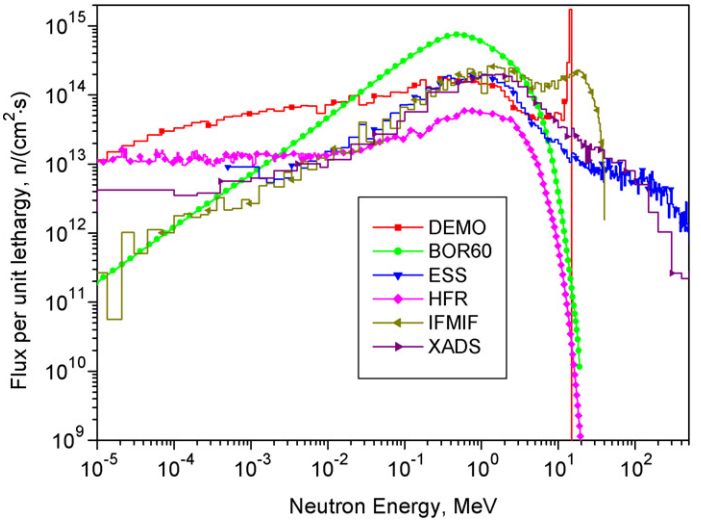

Fig. 9. Neutron spectra in the HCPB blanket of fusion DEMO reactor, the IFMIF high flux test volumes, the spallation sources ESS and XADS as well as of fission reactors HFR (Petten) and BOR-60 (Dimitrovgrad).

Fig. 9. Spectres de neutrons de couvertures tritigènes de type HCPB refroidies à l'hélium du réacteur DEMO, des volumes de test à flux élevé d'IFMIF, des sources de spallation ESS et XADS, ainsi que des réacteurs de fission HFR (Petten) et BOR-60 (Dimitrovgrad).

8.2. Neutron spectra

The neutron spectra of the nuclear facilities considered are presented in Fig. 9. The factor most important for the comparison is the energy range of neutrons covered by each spectrum. The spectra of spallation (ESS and XADS) and stripping (IFMIF) accelerator driven sources have some fraction of neutrons with the energy higher than the characteristic fusion neutron peak at 14.1 MeV. In the ESS the neutron flux in the energy range 5–14 MeV is several times lower than in the DEMO and a neutron tail with energies up to hundreds of MeV is present. The IFMIF spectrum reproduces quite well the shape of the DEMO fusion reactor spectrum already near the 14 MeV peak and at intermediate energies, while the ESS and XADS neutron spectra are an order of magnitude smaller in flux. It should be noted that for the XADS window and, to a lesser extent, for the ESS rigs at the reflector position, a substantial proton flux has to be taken into account for the proper assessment of the material response to irradiation.

8.3. PKA spectra

The $W(T)$ function usually increases smoothly without steps in fusion structural materials (with an exception for ^{6}Li based tritium breeder materials [70]). The hatched area in Fig. 10 shows that the relevant test volume of IFMIF meets perfectly over the entire PKA energy range the DEMO reactor conditions in iron based alloys, because the shape of the $W(T)$ function can be adjusted by using an appropriate combination of W-moderator plates [54].

8.4. Displacement damage and gas production

The data on the displacement damage and the gas production rates for all of the facilities are summarized in Table 2. The maximum values for the DEMO HCPB (at the first wall outboard midplane) are taken from the Ref. [71]. For the ESS and IFMIF High Flux Test Module (HFTM) maximum and minimum values in different irradiation rigs have been calculated. All the data refer to iron as a major component of reduced activated ferritic-martensitic steels presently considered as prime candidate for fusion structural materials.

Even in a typical fast breeder reactor neutron spectrum the He gas to displacement damage ratio is below 1 appm He/dpa, while in a first wall fusion reactor spectrum this ratio is 10–12 appm He/dpa, and in the ADS demon-

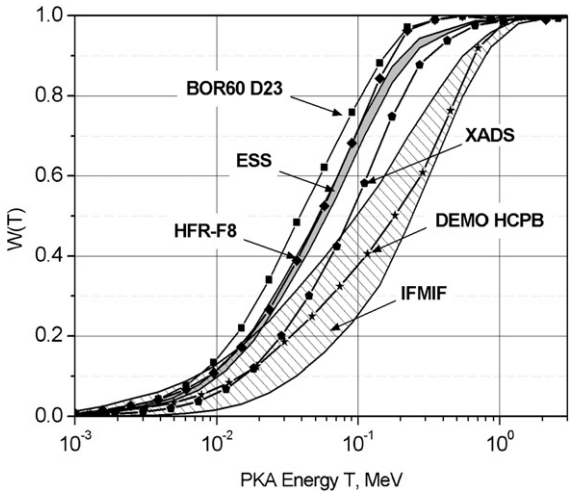

Fig. 10. Damage production function $W(T)$ in iron for HCPB blanket of DEMO reactor in comparison with the stripping neutron source IFMIF (hatched area), neutron spallation sources ESS and XADS, and fission reactors HFR, Petten and BOR-60, Dimitrovgrad.[3]

Fig. 10. Fonction de production de dommage $W(T)$ dans du fer irradié dans les couvertures tritigènes du réacteur DEMO, par les neutrons des réactions de « stripping » d'IFMIF (plage hachurée), par les neutrons de spallation des sources ESS et XADS, et dans les réacteurs de fission HFR de Petten et BOR-60 de Dimitrovgrad.

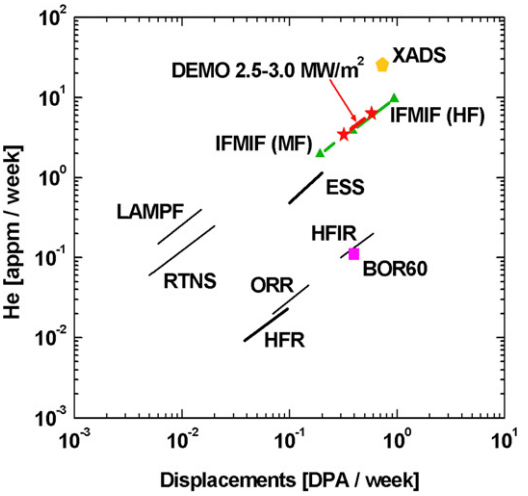

Fig. 11. Ranges of helium and damage production for the DEMO power reactor and for the accelerator driven neutron sources discussed in the paper. For comparison we presented also the data for several other irradiation facilities: Los Alamos Meson Physics Facility (LAMPF) at LANL, Rotating Target Neutron Source (RTNS) at UC Berkeley, Oak Ridge Research Reactor (ORR) and High Flux Isotope Reactor (HFIR) at ORNL.[3]

Fig. 11. Production d'hélium et de dommage pour le réacteur de puissance DEMO et les sources de neutrons discutées dans ce papier. Pour comparaison, nous présentons aussi les données de plusieurs autres installations : Los Alamos Physics Facility (LAMPF) au Laboratoire National de Los Alamos (LANL), Rotating Target Neutron Source (RTNS) à l'Université de Californie Berkeley, Oak Ridge Research Reactor (ORR) et High Flux Isotope Reactor (HFIR) au Laboratoire National d'Oak Ridge (ORNL).

Table 2
Displacement damage and gas production in iron for several neutron irradiation environments[3]

Tableau 2
Dommage de déplacements et production de gaz de transmutation dans le fer pour différents environnements d'irradiation

Irradiation parameter		Demo FW 3 MW/m^2	IFMIF HFTM	ESS irr. rigs reflector	XADS 1MW window	HFR position F8	BOR60 position D23
Total flux, 1/cm^2/s	n	1.3×10^{15}	5.7×10^{14}	6.5×10^{14}	1.2×10^{15}	3.8×10^{14}	2.3×10^{15}
	p	0	0	2.5×10^{12}	2.7×10^{14}	0	0
Damage, dpa/fpy		30	20–55	5–10	38	2.5	20
H, appm/fpy		1240	1000–2400	160–360	16250	1.9	14
He, appm/fpy		320	250–600	25–60	1320	0.8	5.8
H/dpa		41	35–54	33–36	430	0.8	0.70
He/dpa		11	10–12	5–6	35	0.3	0.29

strator it amounts to about 50 appm/dpa (see Fig. 11). Even more sensitive to the high-energy tail of the neutron spectrum is the production of hydrogen isotopes.

As can be seen from Table 2 fission reactors are not adequate for the simulation of fusion irradiation conditions due to the very low gas production rates and low gas to dpa production ratios. The HFTM of IFMIF provides damage and

[3] Reprinted from [55] with permission from Elsevier.

gas production values exactly in the same range as the fusion DEMO reactor. In spite of the fact that the displacement damage produced at the ESS irradiation rigs is about two times lower than for DEMO and IFMIF, the gas to dpa ratios would be still acceptable for the fusion material irradiation. However, the lower damage rate in the ESS implies about two times longer irradiation campaigns to reach the same DEMO relevant irradiation dose (100–150 dpa). In the IFMIF high flux test module the neutron damage ranges from 55 to 20 dpa/fpy in a volume of 0.5 litre, allowing one to one or even accelerated tests of materials for the DEMO fusion reactor. On the other hand, somewhat higher damage is generated in the XADS window and the gas production is too high with respect to the DEMO reactor, due to the simultaneous irradiation by high-energy neutrons and protons.

At the typical ESS irradiation position the total proton flux is about 2.5×10^{12} p/cm^2 s (i.e. only 0.4% of the neutron flux which is about 6.5×10^{14} n/cm^2 s). However, most of the protons ($\sim$97%) have energies far above 15 MeV and thus contribute significantly to the total H and He production. The gas production is increased due to spallation reactions, which produce numerous light elements as debris of the target elements.

The He/dpa ratio in Fe based alloys in the ESS is between 5–6, about a factor of two lower than expected for DEMO, while the H/dpa ratio is about 33–36, which is only a factor of about 1.5 below DEMO. In IFMIF HFTM the He/dpa and H/dpa are 10–12 and 35–50, respectively, and therefore practically identical to the related DEMO values.

8.5. Transmutations

Transmutation occurs as a result of a nuclear reaction when a target nucleus changes its mass and/or charge. Transmutation reactions usually require large energy transfer and are observed under irradiation by neutrons with energy above several MeV. Therefore, a long time irradiation under such conditions might result in the change of the chemical composition of irradiated material. This could have negative consequences for the physical properties of irradiated materials. For example, the major concern for structural materials is degradation of their mechanical properties, which can be induced by irradiation as well as by formation of detrimental elements like phosphor, sulfur and some others. Even small concentrations of such elements can be dangerous due to their pronounced segregation at grain boundaries. Being precipitated on the grain boundaries these elements reduce intergranular cohesion, thus inducing material embrittlement.

Transmutation produces also non-stable nuclei, which emit by decay various types of radiation. Induced activity reduces with time after the end of irradiation, but for some elements this can exceed the safe hands-on level for as long as 100 000 years. This means that common structural materials should be kept, after irradiation, in special storage during this time. Therefore, the development of reduced activation materials was started in the framework of the European Fusion Program. In reduced activation steels, in particular, some elements producing long-living radioactive wastes were replaced by other elements producing shorter lived isotopes. A major concern of this development was to improve mechanical properties of steels, which were obtained by alloying, as well as to enhance their radiation resistance [72].

Spallation reactions induced by high-energy protons and neutrons also generate a huge variety of isotopes starting from the target element down to the light elements including gaseous atoms like helium and hydrogen isotopes (see [68,69]).

Fig. 12 shows that, in spite of the initial concerns, the production of spallation elements in the XADS beam window appears to be not so high as was expected initially. The results of our calculations agree well with the experimental data [75–77] (shown in figure with various symbols). Spallation elements production at the beam window center is about 5 times higher than the volume averaged values shown in Fig. 12 [69]. The annual production of sulfur at the beam window center is close to its initial content in T91, while titanium and cobalt yields slightly surpass it.

The worldwide experience in the development of reduced activation ferritic martensitic steels has shown that a reduction of impurity concentrations of B, P and S to the lowest possible level could significantly reduce the tendency to embrittlement. Therefore, initially purified steels are recommended to withstand the effect of spallation elements for a longer time.

9. Summary

In this contribution we have considered mechanisms of displacement damage production in metals and alloys under neutron and proton irradiation as well as consequent evolution of defects. The differences in the interaction of neutrons

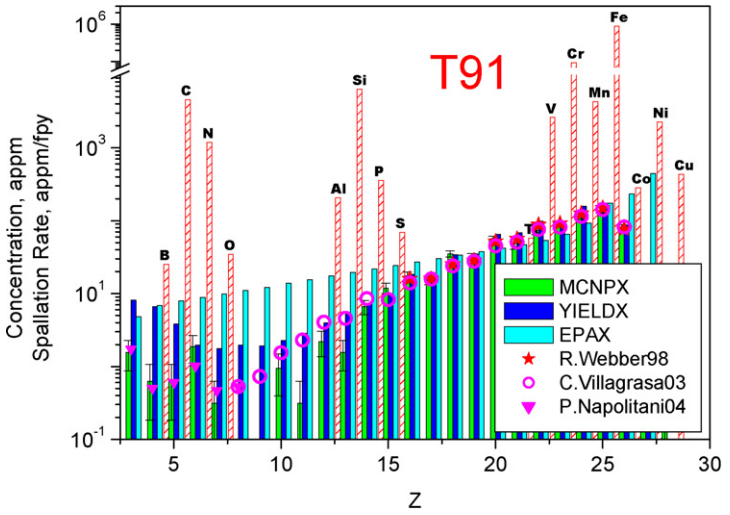

Fig. 12. Spallation element production in the beam window after one year of irradiation as calculated with MCNPX, using two empirical formulae (YIELDX [73] and EPAX [74]) and experimental cross sections from [75–77]. The composition of T91 is shown with red hatched bars.[4]

Fig. 12. Production d'éléments de spallation dans la fenêtre de la cible après un an d'irradiation. Le calcul est fait à partir du code MCNPX en utilisant deux formules empiriques (YIELDX [73] and EPAX [74]) et des sections efficaces expérimentales des références [75–77]. La composition de l'acier T91 est représentée par les barres hachurées en rouge.

and charged particles (including target atom recoils) with solids were discussed. These differences explain why ion irradiation produces different damage morphology from neutron irradiation. In some cases, however, the difference can be tolerated and neutron irradiation can be successfully simulated by ion accelerator irradiation.

We briefly reviewed various theories of displacement damage calculation in monatomic and compound materials and demonstrate their application for assessment of irradiation conditions in various nuclear facilities. We discussed also the implications of these data on mechanical properties of irradiated materials.

Advanced modeling is required to relate more precisely the relationship between neutron spectrum, damage morphology and mechanical properties of irradiated materials.

Acknowledgements

We would like to gratefully acknowledge Professor C.A. English for carefully reading the manuscript and providing us with useful suggestions for improving the paper.

References

[1] V. Heinzel, F. Arbeiter, B. Dolensky, U. Fischer, S. Gordeev, K.H. Lang, D. Leichtle, A. Möslang, S. Simakov, E. Stratmanns, S. Slobodtchouk, P. Vladimirov, Fusion Eng. Design 82 (15–24) (2007) 2444–2450.
[2] B.T. Kelly, Irradiation Damage to Solids, Pergamon Press, 1966.
[3] Yu. Lizunov, A. Möslang, A. Ryazanov, P. Vladimirov, New evaluation of displacement damage and gas production for breeder ceramics under IFMIF, fusion and fission neutron irradiation, J. Nucl. Mater. 307–311 (2002) 1680–1685.
[4] L.R. Greenwood, J. Nucl. Mater. 216 (1994) 29–44.
[5] A.D. Marwick, J. Nucl. Mater. 55 (1975) 259–266.
[6] R. Seber, Phys. Rev. 72 (1947) 1114.
[7] R. Michel, et al., NIMB 103 (1995) 183–222.
[8] M.T. Robinson, J. Nucl. Mater. 216 (1994) 1–28.
[9] S. Klaumünzer, M.-D. Hou, G. Schumacher, Phys. Rev. Lett. 57 (1986) 850.
[10] A. Dunlop, D. Lesueur, P. Legrand, H. Dammak, J. Dural, Nucl. Instr. Meth. B 90 (1994) 330.
[11] F.A. Garner, L.R. Greenwood, P. Roy, An assessment of potential gamma ray enhancement of embrittlement in ABWR pressure vessel walls, in: Effects of Radiation on Materials: 18th Inter. Symp., ASTM STP 1325, pp. 52–74.

[4] Reprinted from [69] with permission from Elsevier.

[12] D.J. Bacon, F. Gao, Yu.N. Osetsky, J. Nucl. Mater. 276 (2000) 1–12.
[13] L.K. Mansur, in: G.R. Freeman (Ed.), Kinetics of Nonhomogeneous Processes, Wiley, New York, 1987, pp. 377–463.
[14] R.S. Averback, R. Benedek, K.L. Merkle, J. Nucl. Mat. 75 (1978) 162.
[15] B.N. Singh, J.H. Evans, J. Nucl. Mater. 226 (1995) 277–285.
[16] R.E. Stoller, in: R.K. Nanstad, M.L. Hamilton, F.A. Garner, A.S. Kumar (Eds.), Effects of Radiation on Materials: 18th. International Symposium, ASTM STP 1325, American Society for Testing and Materials, Philadelphia, 1999, pp. 14–29.
[17] F. Gao, D.J. Bacon, P.E.J. Flewitt, T.A. Lewis, Mat. Res. Soc. Symp. Proc. 439 (1997) 307.
[18] H. Wiedersich, J. Nucl. Mater. 179–181 (1991) 70–75.
[19] C.A. English, Rad. Eff. Def. Solids 113 (1990) 15–28.
[20] J.H. Evans, Phil. Mag. Lett. 87 (8) (2007) 575–580.
[21] Yu.N. Osetsky, D.J. Bacon, Nucl. Instr. Meth. B 202 (2003) 31–43.
[22] M. Kiritani, J. Nucl. Mater. 216 (1994) 220–264.
[23] M. Kiritani, J. Nucl. Mater. 276 (2000) 41–49.
[24] C.A. English, Recoil effects in radiation damage, Rad. Eff. Def. Solids 1 (13) (1990) 15–28.
[25] M. Kiritani, Recoil energy spectrum effects and point defect processes characteristic of cascades, J. Nucl. Mater. 179–181 (1991) 81–86.
[26] M. Kiritani, T. Yoshiie, S. Kojima, Y. Satoh, Rad. Eff. Def. Solids 113 (1990) 75–96.
[27] Y. Satoh, et al., J. Nucl. Mater. 179–181 (1991) 901–904.
[28] P. Vladimirov, et al., J. Nucl. Mater. 250 (1997) 236–241.
[29] E.V. Metelkin, A.I. Ryazanov, Atomic Energy 83 (3) (1997) 653–657.
[30] S. Jumel, J.C. Van-Duysen, J. Nucl. Mater. 328 (2004) 77–261.
[31] G.H. Kinchin, R.S. Pease, Rep. Progr. Phys. 18 (1955) 1.
[32] J.M. Torrens, M.T. Robinson, M.J. Norgett, Phys. Rev. B 9 (1974) 5007.
[33] M.J. Norgett, M.T. Robinson, I.M. Torrens, Nucl. Eng. Des. 33 (1975) 50.
[34] J. Lindhard, V. Nielsen, M. Scharff, P.V. Thornsen, Kgl. Danske Videnskab Seiskab. Mat.-fys. Medd. 33 (10) (1963).
[35] J. Lindhard, V. Nielsen, M. Scharff, Kgl. Darske Videnskab. Selskab, Mat.-fys. Medd. 36 (10) (1968).
[36] J. Lindhard, M. Scharff, H.E. Schidtt, Kgl. Darske Videnskab. Selskab, Mat.-fys. Medd. 33 (14) (1963).
[37] D.M. Parkin, C.A. Coulter, J. Nucl. Mater. 85–86 (1979) 611.
[38] L.R. Greenwood, Radiation Damage Calculations for Compound Materials, September 19–22, 1989, Advisory Group Meeting on Nuclear Data for Radiation Damage Assessment and Related Safety Aspects International Atomic Energy Agency, Vienna, Austria.
[39] J.F. Ziegler, J.P. Biersack, U. Littmark, The Stopping and Range of Ions in Solids, Pergamon Press, Inc., 1985.
[40] M.T. Robinson, I.M. Torrens, Phys. Rev. 9 (1974) 5008; PSR-0137/06: M.T. Robinson, MARLOWE Binary Collision Cascade Simulation Program, Version 15a, A Guide for Users, September 1, 2001.
[41] Yu.D. Lizunov, A.I. Ryazanov, Rad. Eff. 60 (1982) 95.
[42] P.V. Vladimirov, Yu.D. Lizunov, A.I. Ryazanov, Damage calculations in compound materials under neutron and ion irradiation, Rad. Eff. 139 (1996) 109–123.
[43] R.E. MacFarlane, D.W. Muir, R.M. Boicourt, The NJOY Nuclear Data Processing System, vol. I: User's Manual LA-9303-M (ENDF-324), May 1982.
[44] F. Maury, M. Biget, P. Vajda, et al., Anisotropy of defect creation in electron-irradiated iron crystals, Phys. Rev. B 14 (1976) 5303–5313.
[45] ASTM Standard E521, Standard practice for neutron radiation damage simulation by charged-particle irradiation, Annual Book of ASTM Standards, Vol. 12 (2), 1993.
[46] H.H. Anderson, Appl. Phys. 18 (1979) 131–140.
[47] N. Juslin, K. Nordlund, J. Wallenius, L. Malerba, Nucl. Instr. Meth. Phys. Res. B 255 (1) (2007) 75–77.
[48] S. Shimakawa, N. Sekimura, N. Nojiri, Radiation Damage Calculation by NPRIM Computer Code with JENDL3.3, 2002 Symposium on Nuclear Data (JAERI-Conf 2003-006), INDC(JPN)-191/U.
[49] Yu.D. Lizunov, A.I. Ryazanov, Rad. Eff. 60 (1982) 95.
[50] A. Yu. Konobeyev, Yu.V. Konobeev, Yu.A. Korovin, Nuclear Data to Study Damage in Materials under Irradiation by Nucleons with Energies up to 25 GeV, INPPE, Obninsk, November 2000.
[51] M.B. Chadwick, S.C. Frankle, R.C. Little, P.G. Young, Nuclear data libraries for incident neutrons and protons to 150 MeV in ENDF-6 format, in: Proc. of the Topical Meeting on Nuclear Applications of Accelerator Technology, American Nuclear Society, La Grange Park, IL, 1997, pp. 175–182.
[52] M.H. Barnett et al., Calculations of Radiation Damage at SNS, in: Proc. of AccApp'99.
[53] R.E. Prael, H. Lichtenstein, User Guide to LCS: The LAHET Code System. Los Alamos National Laboratory report LA-UR-89-3014, Revised, September 15, 1989.
[54] A. Möslang, P. Vladimirov, Fusion Eng. Design 63–64 (2002) 121.
[55] P. Vladimirov, A. Möslang, Comparison of material irradiation conditions for fusion, spallation, stripping and fission neutron sources, J. Nucl. Mater. 329–333 (1) (2004) 233–237.
[56] R.E. Stoller, J. Nucl. Mater. 276 (2000) 22–32;
D.J. Bacon, et al., J. Nucl. Mater. 276 (2000) 1–12.
[57] R.S. Averback, R. Benedek, K.L. Merkle, Efficiency of defect production in cascades, J. Nucl. Mater. 69–70 (1978) 786–789.
[58] I. Ishida, S. Sasaki, T. Yoshiie, et al., Analysis of the sub-cascade structure in copper produced by ion irradiations, J. Nucl. Mater. 179–181 (1991) 913–916.
[59] D.J. Bacon, Y.N. Osetsky, R.E. Stoller, R.E. Vosloboinikov, MD description of damage production in displacement cascades in copper and a-iron, J. Nucl. Mater. 323 (2003) 152–162.

[60] J.H. Kinney, M.W. Guinan, Z.A. Munir, Defect production efficiencies in thermal neutron irradiated copper and molybdenum, J. Nucl. Mater. 123 (1984) 1028–1032.
[61] U. Fischer, D. Leichtle, H. Tsige-Tamirat, Neutronics Characteristics of a Solid Breeder Blanket for a Fusion Power Demonstration Reactor, in: Annual Meeting on Nucl. Technology, Karlsruhe, ISSN 0720-9207, 1999, p. 553.
[62] Yu. Lizunov, A. Möslang, A. Ryazanov, P. Vladimirov, J. Nucl. Mater. 307–311 (2002) 1680.
[63] A. Möslang, P. Vladimirov, Fusion Eng. Design 63–64 (2002) 121.
[64] U. Fischer, Y. Chen, S.P. Simakov, P.P.H. Wilson, P. Vladimirov, F. Wasastjerna, Overview of recent progress in IFMIF neutronics, Fusion Eng. Design 81 (2006) 1195–1202.
[65] G.S. Bauer, H. Ullmaier, J. Nucl. Mater. 318 (2003) 26–37.
[66] D. King (Chairman), Conclusions of the Fusion Fast Track Experts Meeting, 27 November, 2001.
[67] M. Gasparotto, G. Bauer, G. Martin, A. Möslang, N. Taylor, M. Victoria, Assessment on the Possibility of Neutron Spallation Sources to Contribute to the R&D Programme Related to Material Irradiation Testing, The Fusion Material Irradiation Devices Expert Group, EFDA-T-RE-5.0, September 2002.
[68] P. Vladimirov, A. Möslang, Radiation damage conditions for ESS target hull and irradiation rigs, J. Nucl. Mater. 343 (2005) 205–211.
[69] P. Vladimirov, A. Möslang, Irradiation conditions of ADS beam window and implications for window material, J. Nucl. Mater 356 (2006) 287–299.
[70] Yu. Lizunov, A. Möslang, A. Ryazanov, P. Vladimirov, J. Nucl. Mater. 307–311 (2002) 1680.
[71] S.P. Simakov, U. Fischer, V. Heinzel, U. von Möllendorf, FZK Report, FZKA 6743, 2002.
[72] N. Baluc, et al., Status of reduced activation ferritic/martensitic steel development, J. Nucl. Mater. 367–370 (1) (2007) 33–41.
[73] L. Sihver, C.H. Tsao, R. Silberberg, T. Kanai, A.F. Barghouty, Phys. Rev. C 47 (1993) 1225.
[74] K. Sümmerer, B. Blank, Modified empirical parameterization of fragmentation cross sections, Phys. Rev. C 61 (2000) 034607.
[75] W.R. Webber, et al., Astrophys. J. 508 (1998) 949–958.
[76] C. Villagrasa, et al., J. Phys. IV (France) 12 (2002) Pr8-63.
[77] P. Napolitani, K.-H. Schmidt, A.S. Botvina, F. Rejmund, L. Tassan-Got, C. Villagrasa, Phys. Rev. C 70 (2004) 054607.